

Effect of Al-Si Coating on Weld Microstructure and Properties of 22MnB5 Steel Joints for Hot Stamping

Wenhu Lin, Fang Li, Dongsheng Wu, Xiaoguan Chen, Xueming Hua, and Hua Pan

(Submitted June 23, 2017; in revised form January 11, 2018; published online March 5, 2018)

22MnB5 hot stamping steels are gradually being used in tailor-welded blank applications. In this experiment, 1-mm-thick Al-Si coated and de-coated 22MnB5 steels were laser-welded and then hot-stamped. The chemical compositions, solidification process, microstructure and mechanical properties were investigated to reveal the effect of Al-Si coating and heat treatment. In the welded condition, the coated joints had an Al content of approximately 2.5 wt.% in the fusion zone and the de-coated joints had 0.5 wt.% Al. The aluminum promoted the δ -ferrite formation as the skeletal structure during solidification. In the high-aluminum weld, the microstructure consisted of martensite and long and band-like δ -ferrite. Meanwhile, the low-aluminum weld was full of lath martensite. After the hot stamping process, the δ -ferrite fraction increased from 10 to 24% in the coated joints and the lath martensite became finer in the de-coated joints. The tensile strengths of the coated joints or de-coated joints were similar to that before hot stamping, but the strength of the coated joints was reduced heavily after hot stamping compared to the de-coated joints and base material. The effect of δ -ferrite on the tensile properties became stronger when the fusion zone was soft and deformed first in the hot-stamped specimens. The coated weld showed a brittle fracture surface with many cleavage planes, and the de-coated weld showed a ductile fracture surface with many dimples in hot-stamped conditions.

Keywords δ -ferrite, Al-Si coating, hot stamping, laser welding

1. Introduction

Weight reduction is one of the important issues in vehicle manufacturing. One method is to use advanced high-strength steels (AHSS) and ultrahigh-strength steels (UHSS) (Ref 1). Among these steels, press-hardened steels (PHS), such as 22MnB5 steel, exhibit very high ultimate tensile strength of approximately 1500 MPa after hot stamping (Ref 2). To prevent the surface oxidation and decarburization during the hot stamping process, PHS sheets are usually coated with an Al-Si coating, which can offer good anticorrosion ability and high-temperature oxidation resistance (Ref 3). The other method is to use advanced design, such as tailor-welded blanks (TWBs) (Ref 4). The blanks are welded by a laser beam, which offers flexible delivery, high precision and less thermal distortion and a small HAZ (Ref 5). In comparison, hot-stamped sheets have a softening problem in the heat-affected zone (HAZ) after welding (Ref 6).

The combined utilization of Al-Si coated PHS with TWBs technology provides more weight reduction (Ref 7) and can avoid the HAZ softening (Ref 8). However, the presence of Al-Si coating affects the welding process and the final mechanical properties of the welded joints (Ref 9). It is of great significance to understand the effects of Al-Si coating and adopt a reasonable method to suppress them, instead of introducing costly methods to remove the coating before welding, such as laser ablation (Ref 10), mechanical machining (Ref 11, 12), or the use of arc pretreatment to inhibit Al segregation (Ref 13). Many works have been done on the coating effect in the laser welding of Al-Si-coated hot-stamped sheets. The heat treatment is normally finished, and the Al-Si coating is transformed to intermetallic compounds before welding. They are diluted in the weld pool, causing the Fe-Al intermetallic compounds to segregate along the fusion line (Ref 8). However, limited works have reported the influence mechanism of Al-Si coating during laser welding and the effect of hot stamping on the joints. Kang (Ref 14) investigated TWBs made of dissimilar hot stamping steels (Usibor 1500P and Ductibor 500P). They found that the Al-Si coating led to ferrite formation in the fusion zone, but the tensile strengths of the TWBs were not affected by the coating. They also studied the influence of laser beam radius and hot stamping parameters (Ref 15). When the diameter of the laser beam was smaller, the joint strength after hot stamping became worse.

In this study, Al-Si coated and de-coated 22MnB5 steel sheets are compared in laser-welded and hot-stamped conditions. When the coating remains, the aluminum in the solidification process, microstructure, mechanical properties and failure mode in welded and hot-stamped conditions are discussed in detail. The thermodynamic calculation, solidification morphology and empirical chromium equations will be used to describe the formation of δ -ferrite.

Wenhu Lin, Dongsheng Wu, and Xiaoguan Chen, School of Materials Science and Engineering, Shanghai Key Laboratory of Laser Processing and Materials Modification, Shanghai Jiao Tong University, Shanghai 200240, China; Fang Li and Xueming Hua, School of Materials Science and Engineering, Shanghai Key Laboratory of Laser Processing and Materials Modification, Shanghai Jiao Tong University, Shanghai 200240, China; and Collaborative Innovation Center for Advanced Ship and Deep-Sea Exploration, Shanghai 200240, China; and Hua Pan, Automobile Steel Research Institute, R&D Center, Baoshan Iron & Steel Co., Ltd, Shanghai 201900, China. Contact e-mails: xmhuasjtu@163.com and xmhua@sjtu.edu.cn.

2. Experimental Procedure

2.1 Materials

The Al-Si-coated 22MnB5 steels with a total thickness of 1 mm were provided by ArcelorMittal. The chemical compositions and tensile properties are listed in Table 1. The Al-Si coating (90 wt.% Al, 10 wt.% Si) thickness was 25-30 μm as measured by metallography and an electromagnetic thickness measurer (EPK MINITEST 600). The de-coating preparation was carried out before welding. The top Al-Si layer was removed on both sides using a snap-blade knife (Tajima LC520). The ablation width was 3 mm away from the sheet edge. Figure 1 shows the coating microstructure of the coated and de-coated sheets and the ablation effect. After the ablation, the surface glossiness looked lightly gray. This mechanical removal was abbreviated as MR. The specimens were heated in a furnace at 950 $^{\circ}\text{C}$ for 5 min and water-quenched to room temperature. The base material specimens were named as BM and HSBM for as-received and hot-stamped conditions, respectively.

2.2 Laser Welding Process

Laser welding was performed using an IPG YLS-10000 fiber laser and KUKA robot system. The laser wavelength was 1064 nm. The focus spot diameter was 0.7 mm at the zero defocusing distance. The coated and de-coated sheets were welded using the same welding parameters. The laser power was 2 kW. The welding speed was 5 m/min. The defocusing distance was zero in this experiment. The shielding gas nozzle was 45 $^{\circ}$ tilted along the welding direction. The shielding gas was pure argon (99.9%), with a flow rate of 20 L/min. The laser-welded butt joints were also heated in the furnace at 950 $^{\circ}\text{C}$ for 5 min and subsequently water-quenched. Thus, the specimens were divided into four types: (1) ARW, coated joints, (2) ARW-MR, de-coated joints, (c) ARWHS, coated joints with hot stamping and (4) ARWHS-MR, de-coated joints with hot stamping.

2.3 Metallography and Chemical Analyses

The cross section of the welded joint was cut for the microstructure observations and chemical analyses in Fig. 2(a). The metallography specimens were grit-polished and etched with 4% nital solution (4 mL HNO_3 + 96 mL $\text{C}_2\text{H}_5\text{OH}$). To reveal the solidification microstructure, picric acid solution (4 g picric acid + 100 mL H_2O) was used in a 50 $^{\circ}\text{C}$ water bath for 3 min. The microstructures were characterized by an optical microscope (Zeiss Image A2m) and a scanning electron microscope (FEI Quanta 250). The equilibrium phase evolution and continuous cooling transformation (CCT) diagram were calculated using the software JMatPro. The chemical compositions were analyzed by an energy-dispersive spectrometer (EDS, Oxford Instrument Microanalyses System) and an inductive coupled plasma emission spectrometer (ICP). The

fracture surfaces were observed using a field scanning microscope (FE-SEM, JSM 7600F).

2.4 Mechanical Tests

As shown in Fig. 2(b), the transverse tensile specimens were tested by a universal testing machine (Zwick Z100). The tensile speed was 1 mm/min. To measure the elongation of the welded joints, the gauge length was determined to be 20 mm. Even though elongation is discussed here, the value is only a reference to reveal the ductility difference between the coated and de-coated joints. The micro-hardness was measured using a Zwick ZHV μ Micro Vickers. The sample was loaded with 100 g for 15 s.

3. Results and Discussion

3.1 Coating Microstructure

Figure 1 shows the typical microstructure of the Al-Si coating in the as-received and de-coated conditions. In the as-received condition, the coating had two layers. The top layer was an Al-Si eutectic layer with an average thickness of 25-30 μm , and the intermediate layer was a 6-8 μm Fe-Al intermetallic layer. The intermetallic compounds were considered as Fe_2SiAl_7 , Fe_2Al_5 or FeAl_3 (Ref 16). Si was used to reduce the Al coating thickness by inhibiting the growth of Fe-Al intermetallic layers. The Al-Si layer was soft, and the hard Fe-Al intermetallic layer was not easily removed using the knife in this experiment.

Figure 3 shows the Al-Si coating microstructure after hot stamping. As revealed by the line scanning EDS of the element Al, there were three regions. The different phases were distinguished by the element variation. The chemical compositions in the three different phases are shown in Fig. 3. Region A was a transition layer between the coating and the base steel. Based on the compositions (8.6% Al, 2.36% Si and Fe balance), region A was considered to be $\alpha\text{-Fe}(\text{Al}, \text{Si})$. Regions B and C had Al content of over 20 wt.%. They were Fe-Al intermetallic compounds. According to the formula $n(\text{Al}):n(\text{Fe}) \approx 2 \times (w(\text{Al}):w(\text{Fe}))$, the atom ratio of Al to Fe was obtained by the weight content. The ratio was approximately 2.5(Fe_2Al_5) in region B and 1.0(FeAl) in region C. During the heat treatment, pores and cracks were also formed in the coating, induced by the diffusion, oxidation and thermal stress.

3.2 The Microstructure of the Welded Joints

The previous discussions on δ -ferrite formation and its quantitative effect on mechanical properties were mainly in stainless steels and high-temperature steels, such as 9-12% Cr steels (Ref 17). The delta ferrite was generated in martensite during the hot working process or in service. It was relative to the high Cr content. In this Fe-Cr-(Ni)-C system, the delta

Table 1 Chemical compositions (wt.%) and tensile properties of 22MnB5 steel

Chemical compositions					Tensile properties				
C	Si	Mn	Al	Ti	B	Cr	Fe	R_m , MPa	A_{gt} , %
0.23	0.27	1.13	0.037	0.038	0.0025	0.16	Bal.	582	17

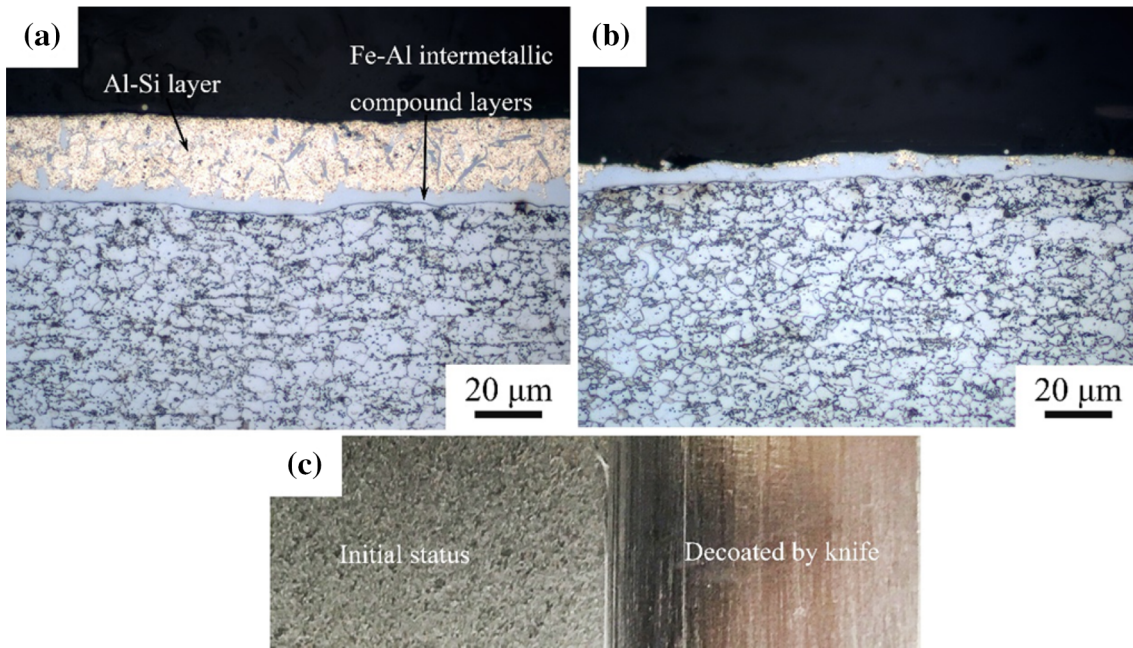


Fig. 1 Al-Si coating microstructure: (a) coated and (b) de-coated sheets and (c) ablation effect

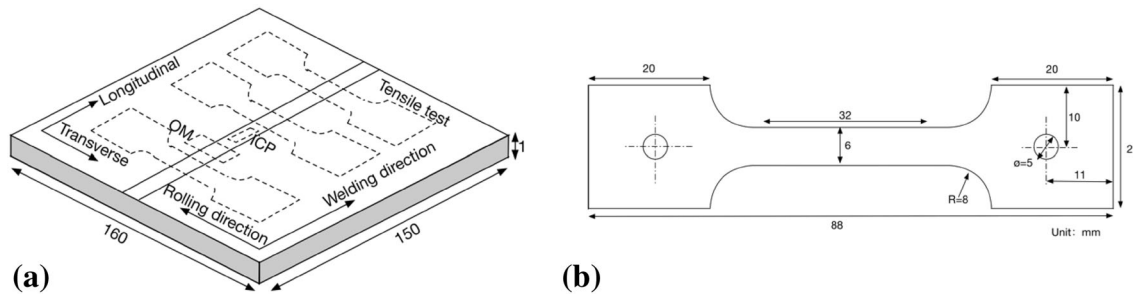
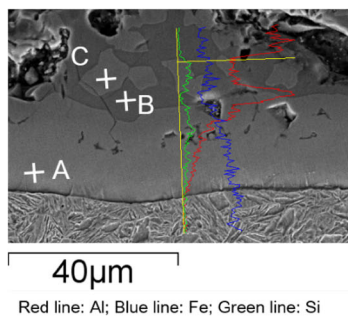


Fig. 2 Schematic diagrams: (a) sampling position and (b) tensile test specimen size



Wt. %	A(α -Fe(Al,Si))	B(Fe_2Al_5 (Si))	C(FeAl(Si))
Al	8.60±0.36	52.42±0.04	29.5±0.90
Fe	89.02±0.46	46.46±0.15	64.84±1.00
Si	2.36±0.08	1.11±0.11	5.66±0.13

Fig. 3 Morphology of Al-Si coating layers and chemical compositions in hot-stamped condition

ferrite affected the phase transformation (Ref 18). The elements Cr and Ni showed strong segregations between austenite and ferrite. In addition, many carbides tended to appear due to the existence of Cr. The martensite and delta ferrite were thus distinguished by the chemical compositions of chromium or nickel. The different fractions of delta ferrite could be obtained for high-Cr steels by heating at different temperatures or modifying the chemical compositions. The cooling rate also resulted in different fractions of delta ferrite in welding (Ref

19). The aluminum and manganese contents were still at low levels even though the coating was melted into the fusion zone. Here, the welded joints with or without delta ferrite were compared to the preferred condition in industry of approximately 950 °C for 5 min.

Figure 4(a) shows the coated welded joints. Figure 4(c) shows the de-coated welded joints. They both had an X-shape or “hourglass” weld profile in keyhole mode laser welding. The keyhole was formed due to the high energy density

($> 10^6$ W/cm²). When the keyhole depth reached above the sheet thickness, the laser beam would go through the weld pool and the keyhole was periodically open on both sides. The metal vapor ejected out from both sides. The heating by plasma on both sides led to this weld shape. In the welding process, the melted coating would float on the upper surface of the molten pool and flow with the molten pool flow.

Even though the Al coating had high heat conductivity, the width of the heat-affected zone (HAZ) was not affected much at the same welding parameters. The HAZ microstructure was also similar in these two joints. Figure 5 shows the HAZ microstructure in the different zones of Fig. 4(a): (a) coarse grain heat-affected zone (CG-HAZ), (b) fine grain heat-affected zone (FG-HAZ), (c) dual-phase transition zone. The as-received microstructure was α -ferrite and pearlite. Under welding thermal cycles, the period with the temperature over A_{c3} was longer in the CG-HAZ than in the FG-HAZ and the austenite grain grew larger. During the cooling period, the cooling rate was very high at over 30 K/s in the HAZ. The austenite would transform into lath martensite. Figure 5(a) indicates the packets and blocks structure in the lath martensite, and they were clearer in the CG-HAZ than in the FG-HAZ. The blue band in Fig. 4(a) was the dual-phase transition zone. It was caused by the lower temperature between A_{c1} and A_{c3} , and part of the primary microstructure ($\alpha + P$) transformed to austenite. Figure 5(c) shows the zone mixed with the martensite and

primary base microstructure. Figure 4(b) and (d) shows the welded joints in hot-stamped condition. The HAZ was missing because the microstructure changed into the same lath martensite microstructure after austenization heating over A_{c3} and water quenching.

Figure 6 presents the fusion zone microstructures indicated by the red boxes in Fig. 4. Figure 6(a) and (b) shows the fusion zone microstructures of the coated specimens. There existed a dual-phase microstructure with a white phase and a dark phase. The dark phase was considered as the lath martensite. The formation of the white phase will be discussed in the later paragraphs. Using the software Proimaging, the white-phase fractions were approximately 10 and 24%, respectively, in the welded and hot-stamped conditions. Figure 6(c) and (d) shows the fusion zones in the specimens ARW-MR and ARWHS-MR. They were always lath martensite except for the difference of size. The lath martensite was finer after hot stamping. After the mechanical ablation, only a very thin intermetallic layer remained on the surface. The fusion zone microstructures from SEM analysis are shown in Fig. 7 and 8. The lath martensite structure was clearly demonstrated, and the second phase was shown with an irregular boundary. The second phase had an island shape or dendrite grain boundary. After hot stamping, the coarse band-like second phase was still there and some white phases were formed inside the martensite. They were possibly the α -ferrite.

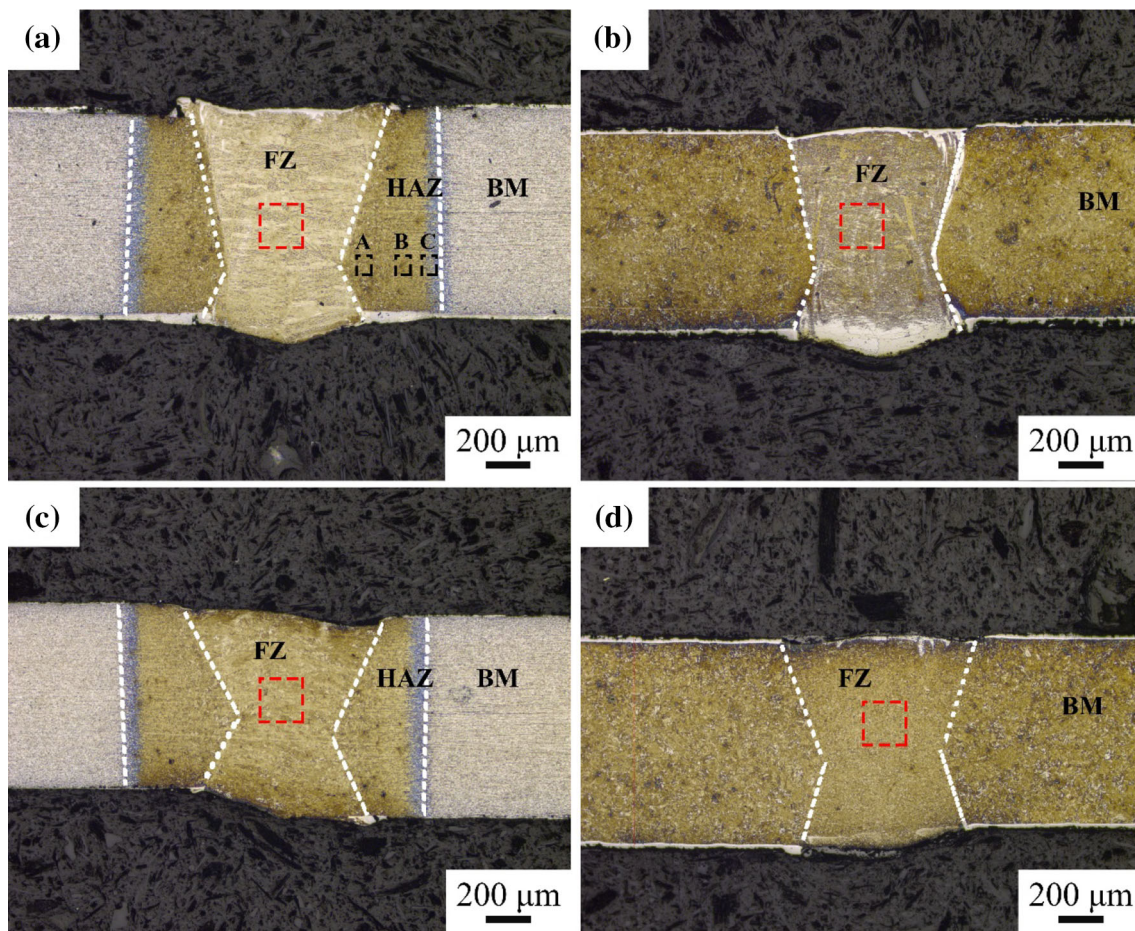


Fig. 4 Fiber laser-welded joints in different conditions: (a) as-received welded joint with coating (ARW); (b) as-received welded and hot-stamped joint with coating (ARWHS); (c) as-received welded joint with mechanical removal of coating (ARW-MR); (d) as-received welded and hot-stamped joint with mechanical removal of coating (ARWHS-MR)

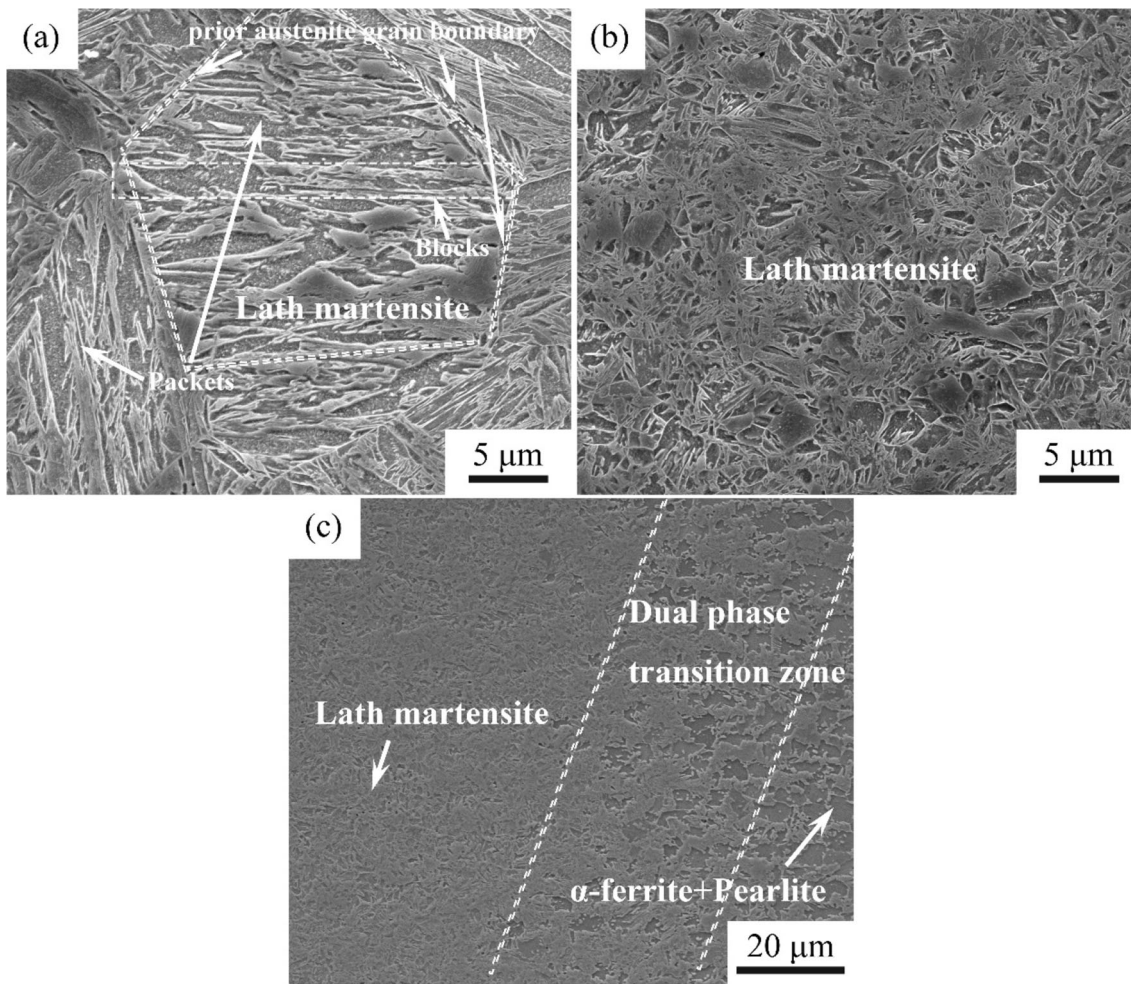


Fig. 5 SEM microstructure of the HAZ shown in the black box in Fig. 4(a): (a) CG-HAZ; (b) FG-HAZ; (c) dual-phase transition zone

The later EDS result revealed that the average Al content was approximately 0.5 wt.% in the fusion zone. The CCT diagrams of the base material and that with 0.5 wt.% Al were calculated by JMatPro in Fig. 9. Based on the grain growth formula $D^a = C \cdot t \cdot \exp(-Q/RT)$, the austenite grain size could be estimated. It was approximately 30 μm at 950 $^{\circ}\text{C}$ for 300 s with the parameters $a = 4$, $C = 0.4948 \times 10^{14} \text{ mm}^4/\text{s}$, $Q/R = 63,900$. Thus, the CCT diagrams were calculated with an austenite grain size of 30 μm and an initial cooling temperature from 950 $^{\circ}\text{C}$. The martensite transformation easily occurred when the cooling rate was over 100 K/s. The cooling rate was rapid during laser welding (10^5 K/s) (Ref 20) or water quenching (1276 K/s) (Ref 21). Thus, the martensite can reasonably form in the fusion zones (Fig. 6c and d). The difference was the source of lath martensite. One was transformed from the columnar dendritic austenite grains after welding, and the other was from the recrystallized austenite during hot stamping. The dendritic grain boundaries had high energy where the recrystallization nucleation occurred first. During the high-temperature heating process, the dendritic austenite grain was changed to a smaller equiaxed grain. This led to the finer lath martensite in Fig. 6(d).

3.3 Chemical Compositions and Microstructure Evolutions

To understand the microstructure evolution, the chemical compositions in the fusion zone are listed in Table 2. The spot

EDS analyses were conducted at the top, middle and bottom of the fusion zone. The ICP results provided the average compositions of the fusion zones. The Al and Si contents were higher in the ARW (Al 2.5 wt.%; Si 0.71 wt.%). In comparison, the ARW-MR had lower Al and Si contents (Al 0.5 wt.%; Si 0.46 wt.%). The Al-Si layer played a more important role in the Al and Si contents than the thinner intermetallic compound layer. The Mn content was approximately 1.1 wt.% because the coating did not have Mn. Figure 10 indicates the chemical compositions in the martensite and the second phase. The compositions (wt.) were different: 1.86% Al, 0.71% Si and 1.57% Mn in the martensite and 2.34% Al, 0.70% Si and 1.26% Mn in the second phase. The result indicated that the second phase was not a Fe-Al intermetallic phase. The Al content was lower than the minimum content in Fe-Al intermetallic compounds (12 wt.% for Fe_3Al). The second phase was possibly ferrite rich in Al.

To explain the formation of the second phase, the solidification process was investigated. Figure 11 shows the calculated phase fractions in an equilibrium condition. The calculations were based on the chemical compositions Fe-0.23C-1.18Mn-0.48Si-0.0025B with different Al(0.5 or 2.5 wt.%). Figure 11(a) shows the solidification process with low Al in the equilibrium condition: $L \rightarrow L + \delta \rightarrow L + \delta + \gamma \rightarrow \gamma$. The final microstructure was full of austenite when the solidification was finished. Figure 11(b) shows the solidification process with high Al in

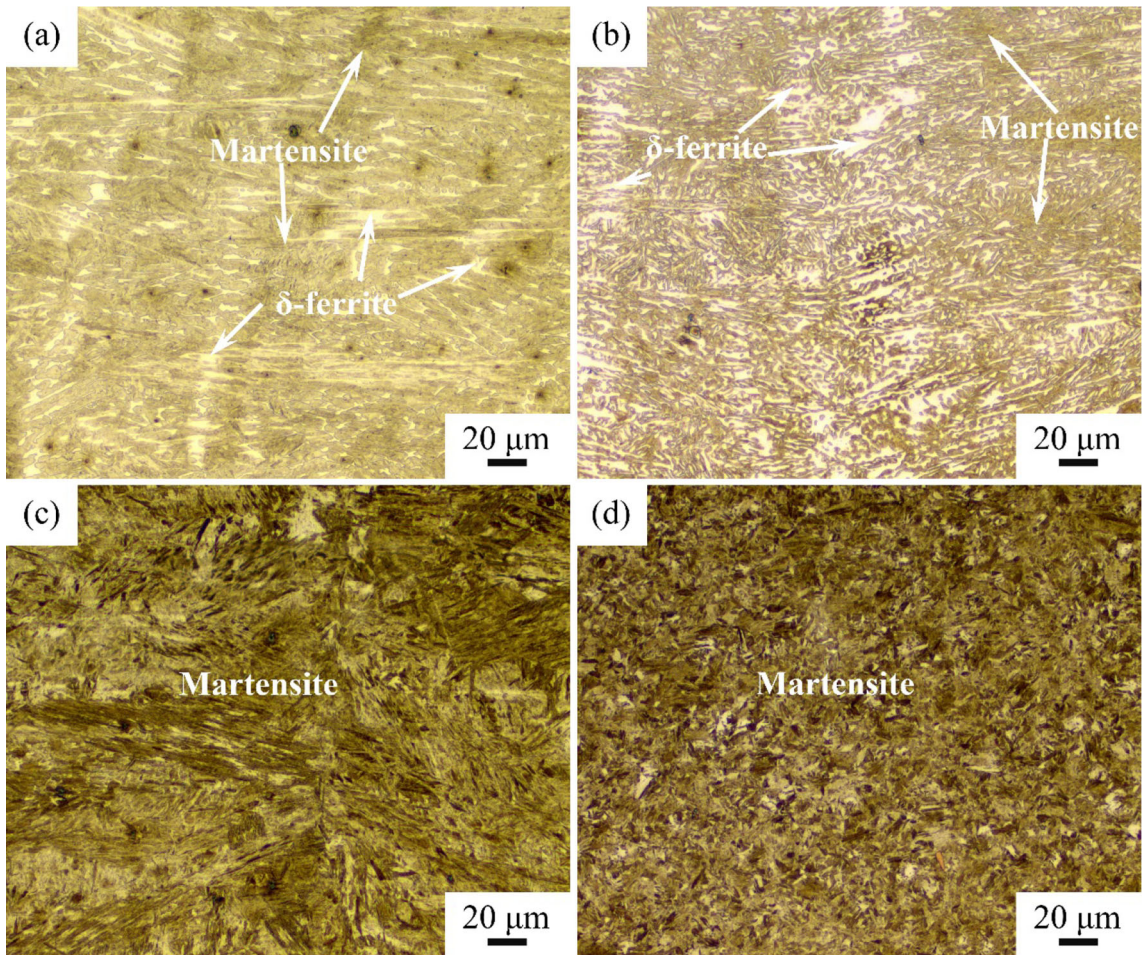


Fig. 6 Weld microstructure in coated joints (a) ARW, (b) ARWHS and de-coated joints (c) ARW-MR, (d) ARWHS-MR

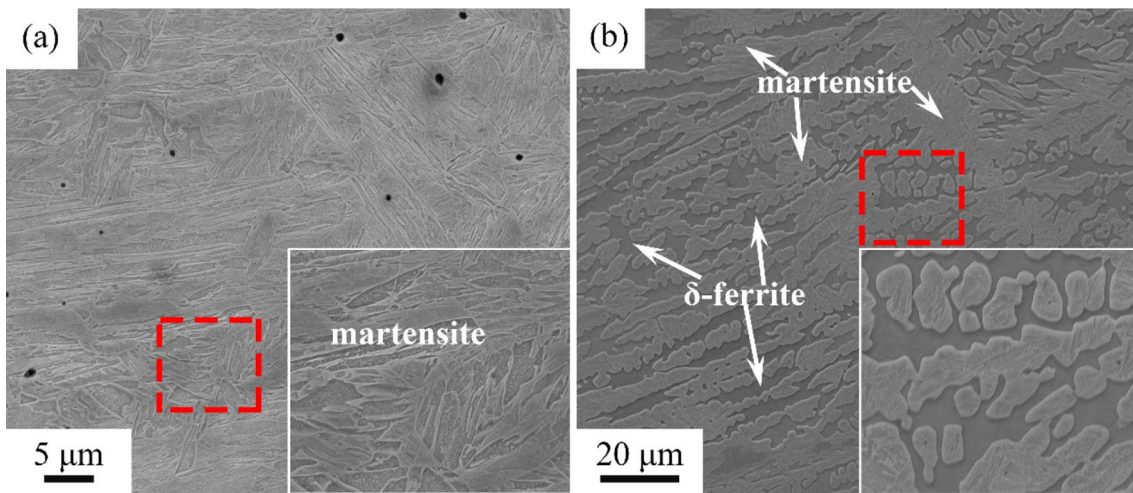


Fig. 7 SEM fusion zone microstructure in the welded condition: (a) ARW-MR, (b) ARW

equilibrium condition: $L \rightarrow L + \delta \rightarrow L + \delta + \gamma \rightarrow \gamma + \delta$. The final microstructure was a dual phase of lath martensite and δ -ferrite. They both indicated that the δ -ferrite was first solidified from the weld pool and then the peritectic reaction continued ($L + \delta \rightarrow \gamma$). When the solidification finished, the high-Al weld

consisted of austenite and δ -ferrite at high temperature. As we all know, δ -ferrite is stable at high temperature (Ref 18). With the temperature further cooling down rapidly, the austenite transformed to martensite and the δ -ferrite remained with the solidification morphology. The non-equilibrium morphology

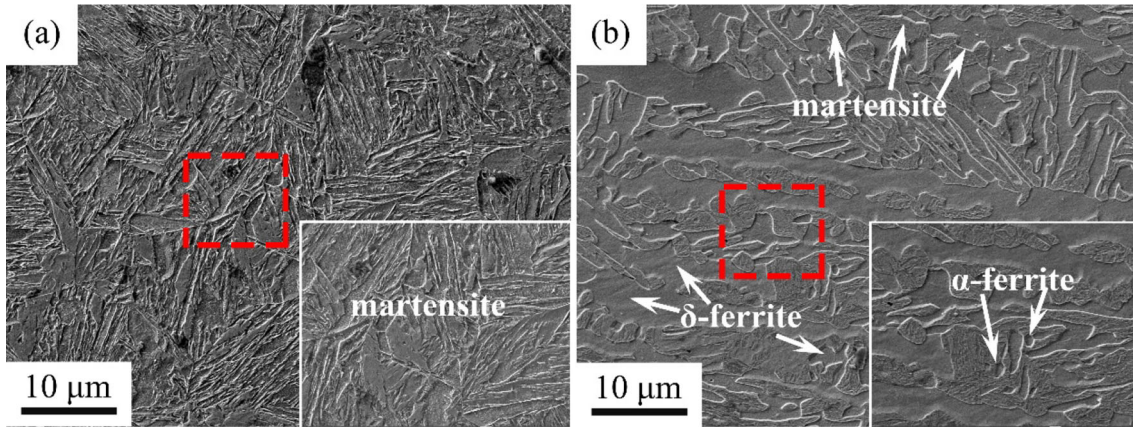


Fig. 8 SEM microstructure in fusion zones after hot stamping: (a) ARWHS-MR, (b) ARWHS

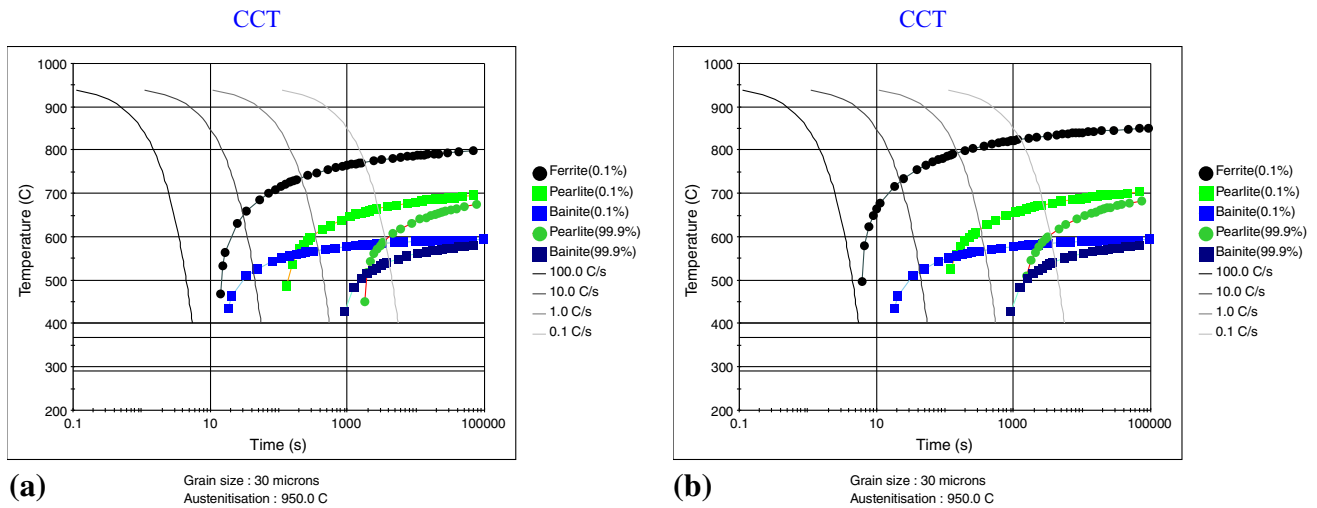


Fig. 9 CCT diagrams of (a) base material 22MnB5 and (b) 22MnB5 with 0.5 wt.% Al

Table 2 Chemical compositions (EDS and ICP) in the fusion zone (wt.%)

ARW	Al	Si	Mn	Fe	ARW-MR	Al	Si	Mn	Fe
EDS					EDS				
Top	2.58	0.77	1.18	95.47	Top	0.49	0.44	1.05	98.03
Middle	2.45	0.63	1.13	95.79	Middle	0.67	0.48	1.06	97.79
Bottom	2.53	0.74	1.15	95.58	Bottom	0.53	0.46	1.12	97.88
Average	2.52	0.71	1.15	95.61	Average	0.56	0.46	1.08	97.9
ICP result	2.102	0.4976	1.056	Bal.	ICP result	0.5696	0.3674	1.063	Bal.

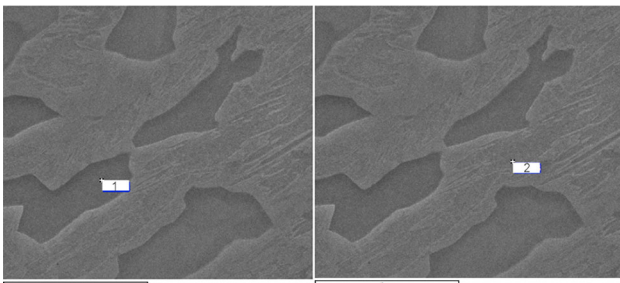


Fig. 10 Spot EDS analyses in different phases of ARW weld (Point 1: the second phase; Point 2: the martensite)

was a skeletal dendritic microstructure with irregular boundaries. Thus, the second phase with the solidification morphology in the fusion zone was δ -ferrite.

The above discussion was presumed in an equilibrium condition. The synchrotron radiation technique showed that the solidification process was in non-equilibrium conditions. The austenite was first solidified from the weld pool in the low-Al weld (Ref 22). The solidification process ($L \rightarrow L + \gamma$) became different in the non-equilibrium condition. In the high-Al weld with 3.7 wt.% Al, Babu (Ref 23) proved that the solidification process was still primarily δ -ferrite formation at a cooling rate of 1500 K/s. This was in agreement with the calculated solidification process ($L \rightarrow L + \delta$) in high-Al weld.

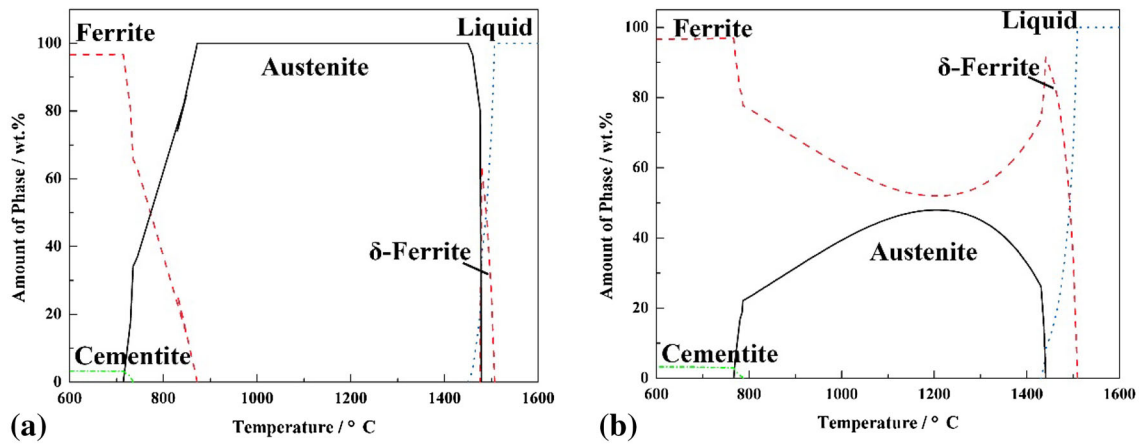


Fig. 11 Calculated phase fractions at the equilibrium condition: (a) 0.5 and (b) 2.5 (wt.%) Al

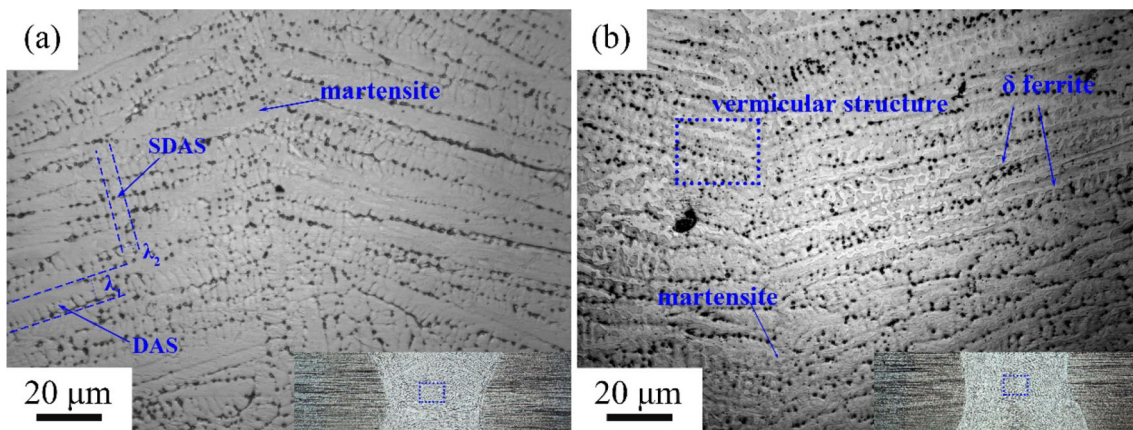


Fig. 12 Solidification microstructure etched by picric acid in a 50 °C water bath for 3 min: (a) ARW-MR, (b) ARW

Figure 12 shows the solidification microstructure etched by picric acid. The cooling rate (ε) was estimated according to the dendrite arm spacing (DAS, λ_1) and the secondary dendrite arm spacing (SDAS, λ_2) in Fig. 12. λ_1 and λ_2 were approximately 15 and 3.3 μm , respectively. The empirical equation to predict the cooling rate was used even though it was used in 310 stainless steel (Ref 24). Based on the above equations, the cooling rate ε was 1072 and 1382 K/s, respectively. The cooling process was very fast in the weld pool.

$$\lambda_1 = 80(\varepsilon)^{-0.33},$$

$$\lambda_2 = 25(\varepsilon)^{-0.28}.$$

To determine the solidification process in the non-equilibrium condition, Elmer (Ref 25) summarized the mapping relationship between morphologies and solidification modes. Figure 12(a) shows that there was very little δ -ferrite remaining in the dendritic grain boundaries. This morphology was considered as primarily austenite solidification mode. Figure 12(b) shows that the vermicular morphology was primarily ferrite solidified from the weld pool. Except for the morphology, many chromium equivalent equations were also employed to predict the solidification mode in stainless steels. The elements Ni and Cr were mainly considered in stainless steels.

However, the fusion zones here were mainly composed of the elements Al, Mn and Si. Cr, Al and Si were the former elements of ferrite, and Ni and Mn were both the former elements of austenite. The metallurgical effect of Al and Mn was similar to that of Cr and Ni. Based on the fact, the Al-containing chromium equivalent could be used to predict the solidification mode of the Fe-Al-Mn-C weld. Lee (Ref 26) used the following empirical chromium equivalent to reveal the solidification mode of Fe-9.33Mn-5.6Al-0.2C.

$$\text{Cr}_{\text{eq}}(\text{wt.}\%) = 1[\text{Cr}] + 1[\text{Mo}] + 1.5[\text{Si}] + 5.5[\text{Al}],$$

$$\text{Ni}_{\text{eq}}(\text{wt.}\%) = 1[\text{Ni}] + 30[\text{C}] + 25[\text{N}] + 0.5[\text{Mn}].$$

The ratio of Cr_{eq} and Ni_{eq} indicated different solidification modes. They were generally categorized into the following four modes:

A mode: $L \rightarrow L + \gamma \rightarrow \gamma$	$\text{Cr}_{\text{eq}}/\text{Ni}_{\text{eq}} < 1.25$
AF mode: $L \rightarrow L + \gamma \rightarrow L + \gamma + \delta \rightarrow \gamma + \delta$	$1.25 < \text{Cr}_{\text{eq}}/\text{Ni}_{\text{eq}} < 1.48$
FA mode: $L \rightarrow L + \delta \rightarrow L + \delta + \gamma \rightarrow \gamma + \delta$	$1.48 < \text{Cr}_{\text{eq}}/\text{Ni}_{\text{eq}} < 1.95$
F mode: $L \rightarrow L + \delta \rightarrow \delta \rightarrow \gamma + \delta$	$1.95 < \text{Cr}_{\text{eq}}/\text{Ni}_{\text{eq}}$

The empirical chromium and nickel equivalents were calculated according to the average EDS values in Table 2 and the carbon content (0.23 wt.%). The de-coated welds (ARW-MR) had a ratio of $\text{Cr}_{\text{eq}}/\text{Ni}_{\text{eq}}$ equal to 0.53, with 3.77/7.14. The ratio

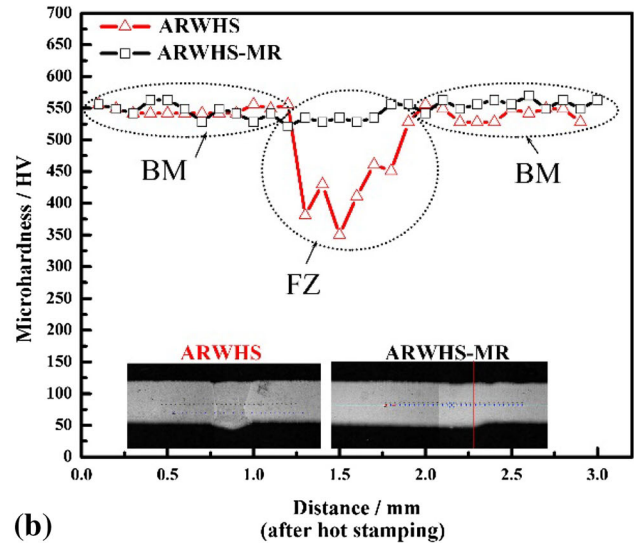
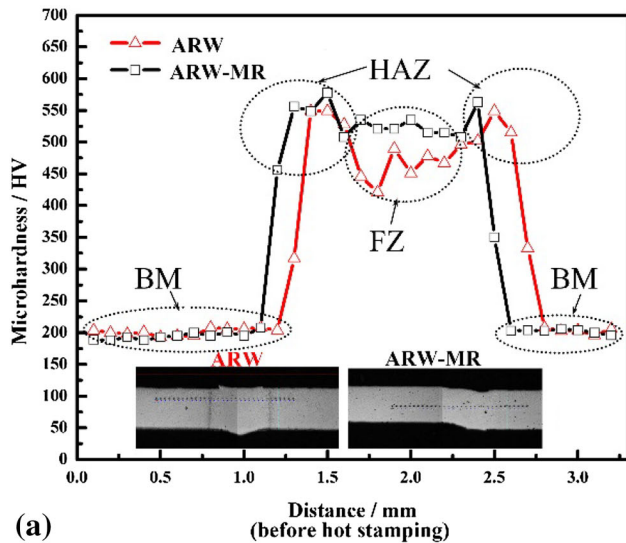


Fig. 13 Micro-hardness distributions across the laser-welded joints: (a) ARW and ARW-MR, (b) ARWHS and ARWHS-MR (the red line represents the coated joint and the black line represents the de-coated joint)

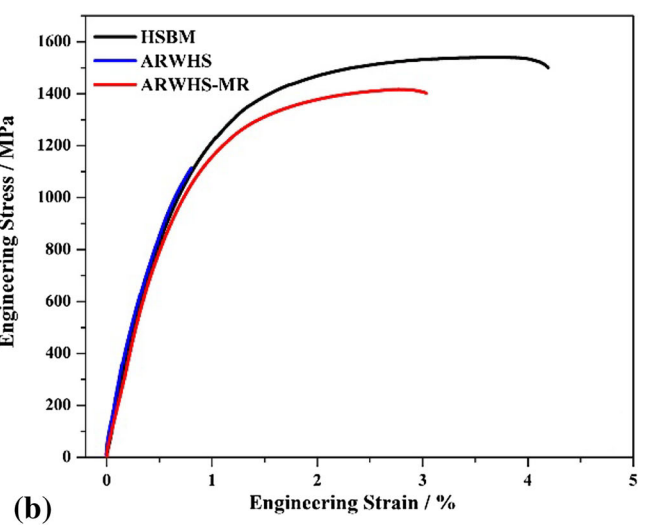
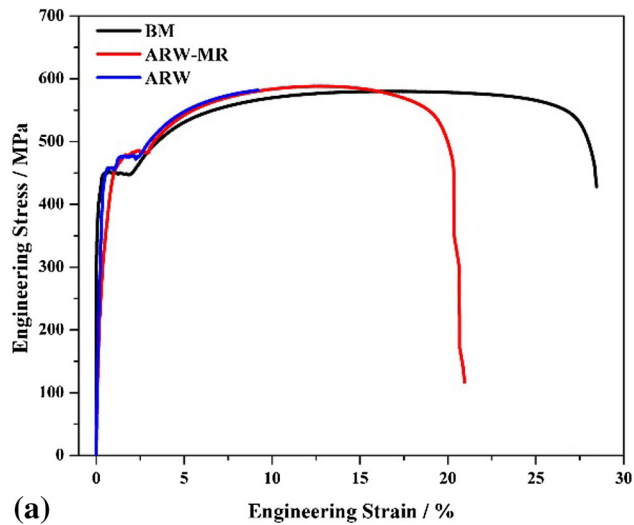


Fig. 14 Tensile properties of the welded joints in (a) as-received welded (ARW) and (b) hot-stamped (HS) conditions (BM: base material; HSBM: hot-stamped base material)

was in agreement with the A mode ($L \rightarrow L + \gamma \rightarrow \gamma$). For the high-Al weld, the ratio was 14.925/7.175, approximately 2.08. The ratio exceeded the upper limit (1.95). The F mode solidification was suitable in the high-Al weld. Therefore, the morphology and equivalent chromium equation had the same conclusions: $L \rightarrow L + \delta \rightarrow \delta \rightarrow \gamma + \delta$ in ARW, $L \rightarrow L + \gamma \rightarrow \gamma$ in ARW-MR. They were both acceptable to determine the solidification mode in non-equilibrium condition.

3.4 Mechanical Properties

The effect of delta ferrites on the mechanical properties examined included the tensile properties (Ref 27) and impact properties (Ref 28) in stainless steels with high Cr. The delta

ferrites caused a decrease in strength in martensitic stainless steels regardless of whether the carbides were considered. There were few investigations on the delta ferrite effect on the mechanical properties of the martensitic microstructure of the Fe-Mn-Al-C system.

3.4.1 Micro-hardness. Figure 13 shows the micro-hardness distributions across the four different specimens. Figure 13(a) indicates the hardness curves of ARW and ARW-Mr. The hardness curves were divided into three regions: FZ, HAZ and BM. The BM hardness value was approximately 200 HV. In this softest zone, the microstructure was ferrite and pearlite. The maximum hardness was located in the HAZ, which was caused by the large fraction of martensite. For the de-coated

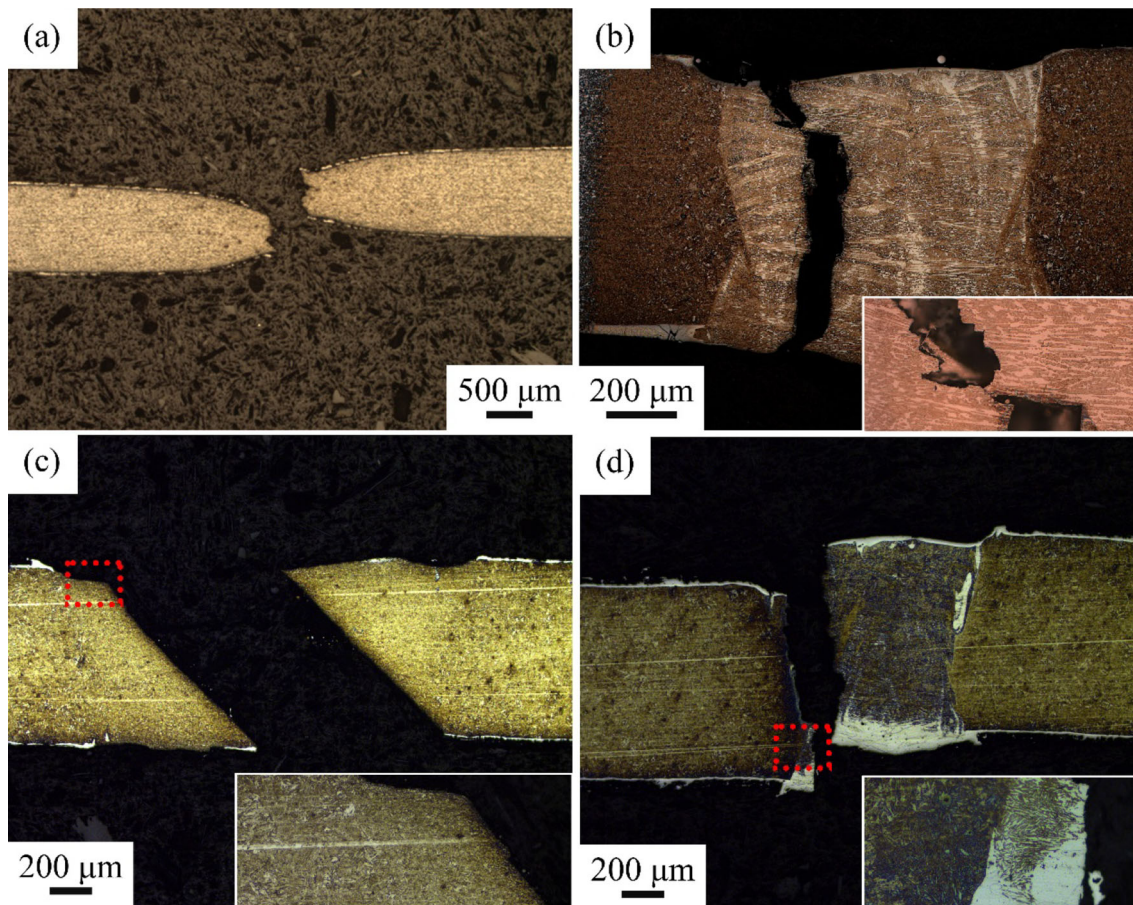


Fig. 15 Failure locations in different tensile specimens: (a) ARW-MR; (b) ARW; (c) ARWHS-MR; (d) ARWHS

specimen, the FZ also consisted of full martensite. The hardness of HAZ and FZ was approximately 550 and 530 HV, respectively. When the coating remained, the FZ hardness had a non-uniform reduction. The minimum hardness of the fusion zone was 400 HV. Comparing the microstructures of the two fusion zones ARW and ARW-MR, the reduction came from the δ -ferrite phase. The δ -ferrite had a lower dislocation density than the martensite. Plastic deformation more easily appeared in the δ -ferrite, and thus the hardness decreased.

The hot-stamped specimens are presented in Fig. 13(b). The BM hardness increased to approximately 550 HV. Even though the martensite of the fusion zone in ARWHS-MR seemed finer than that in ARW-MR, the hardness showed little change. However, the ARWHS specimen showed a larger loss of the hardness in the FZ. The minimum hardness was approximately 340 HV. This was caused by the increased ferrite fraction in the coated weld after hot stamping. Therefore, the weakness of the welded joints after hot stamping was located in the FZ.

3.4.2 Tensile Properties and Failure Position. Figure 14(a) compares the tensile properties of BM, ARW and ARW-MR specimens. The difference of the ultimate tensile strength was very small among these welded joints with or without coating. They were all approximately 585 MPa. The uniform elongation was different: BM specimen (17%), coated joints (11%) and de-coated joints (13%). The microstructure in

the both HAZ and FZ included lath martensite. The phase had a higher strength and less deformation ability than the dual phase of α -ferrite and pearlite. Thus, the BM zone would yield first and when the loading force reached over the ultimate tensile strength of BM, the HAZ and FZ in the joints hardly yielded. Therefore, necking always appeared in the BM zone. The less deformation between the gauge lengths eventually resulted in the small elongation. However, part of the ARW specimens failed in the FZ and the cleavage facets were displayed in the fracture surface. This was due to the inhomogeneous fusion zone microstructure. A part of the region in the fusion zone was full of a continuous band-like δ -ferrite phase. This would also yield and break up.

Figure 14(b) shows the tensile properties of the welded joints in hot-stamped condition. The HSBM specimen had an ultimate tensile strength of approximately 1528 MPa and a uniform elongation of approximately 3.7%, which was expected from the full martensite. However, for the ARWHS specimen, due to the existence of δ -ferrite, the ultimate tensile strength decreased to 1124 MPa (73% of BM) and the uniform elongation reduced to 0.9%. Its tensile curve showed very little plastic deformation. This was a typical brittle fracture. The reduction was explained by the mixture of martensite, δ -ferrite and α -ferrite in the FZ. The microstructure was softer than the martensite in the BM. Compared to the specimens in the welded condition, the loading force would first reach the

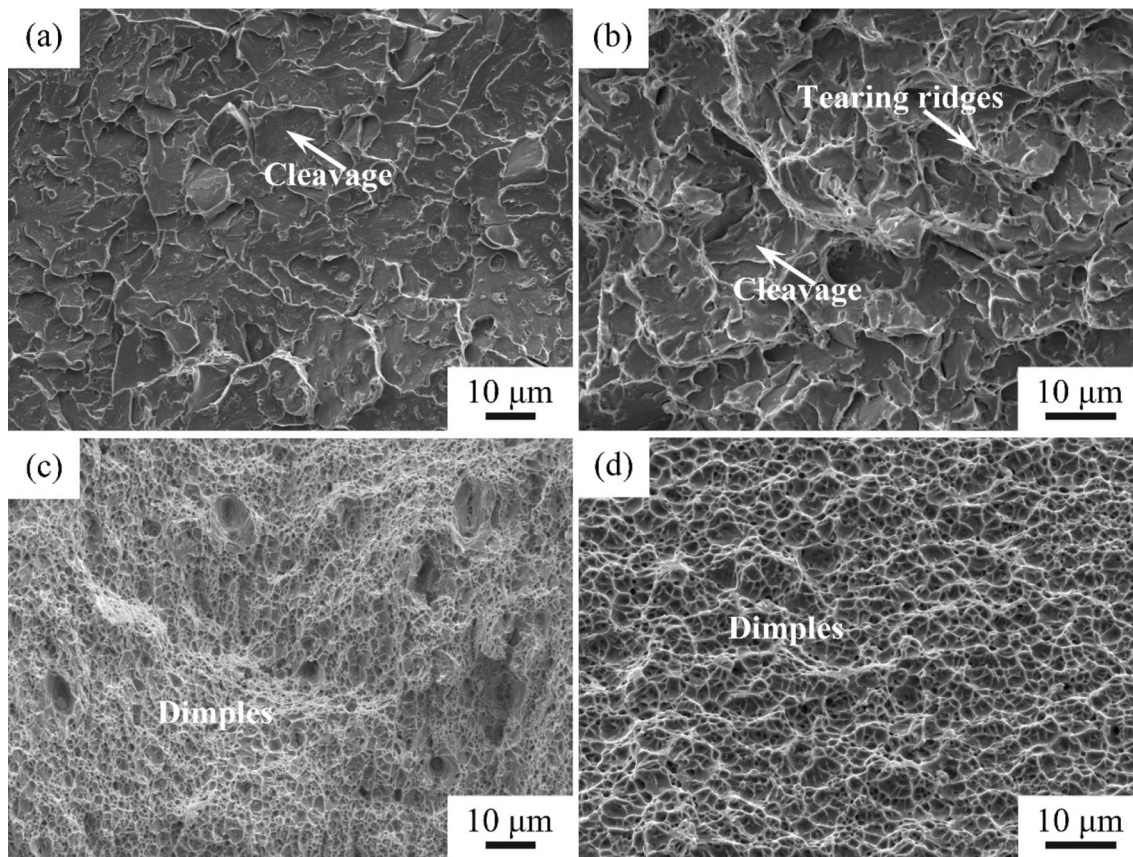


Fig. 16 Fracture surfaces of the welded joints in different conditions. (a) ARW (some failed in FZ), (b) ARWHS (all failed in FZ), (c) ARW-MR (all failed in BM), (d) ARWHS-MR (all failed in FZ)

yielding strength of the FZ. In the fusion zone, δ -ferrite and α -ferrite were softer than the martensite. In addition, the δ -ferrite phase had curly boundaries with a sharp angle. The stress concentration was serious at the sharp corner point. The crack tended to generate first in the δ -ferrite. The δ -ferrite phase was usually long band-like and continuous. The crack was propagated rapidly in this soft δ -ferrite. The deformation of FZ was very small. Before entering into the yielding period of the martensite, the fracture crack had already occurred in the FZ. The total deformation of the ARWHS specimen was extremely small. In previous results (Ref 29), a 1.5-mm-thick sheet had a tensile strength of welded joints that was 90% of the BM strength. The thinner sheet was more sensitive to the coating.

The ARWHS-MR specimen had an ultimate tensile strength of approximately 1428 MPa and a uniform elongation of approximately 3%. The tensile curve indicated that both elastic and plastic deformation existed. The yielding process was similar to that of the martensite microstructure of the HSBM specimen. After hot stamping, the HAZ and FZ transformed to lath martensite. Even with a finer microstructure, the FZ with a small thickness loss had a slightly lower strength than the specimen HSBM.

Figure 15 demonstrates the different failure locations. All of the ARW-MR specimens failed in the BM (Fig. 15a). Some of the ARW specimens failed in the FZ (Fig. 15b). The fracture paths were straight. There was no obvious necking near the failure location. Figure 15(c) shows that the failure of the ARWHS-MR specimen was located in the FZ. The necking occurred near the failure location. The fracture path was 45° to the sheet surface. Figure 15(d) shows that the ARWHS specimen failed in the FZ.

Figure 16 displays the fracture surfaces. Figure 16(a) shows that many cleavage facets existed in the ARW fracture surface. Figure 16(b) shows there were cleavage facets and tearing ridges in the ARWHS specimen. The joint with the cleavage facet was brittle. Figure 16(c) shows that the ARW-MR specimen had many dimples in the fracture surface. Figure 16(d) shows that the fracture surface of the ARWHS-MR specimen also consisted of dimples. The dimple was considered ductile. The Al-Si coating caused the joint to be more brittle, which was in agreement with the low elongation.

4. Conclusions

- (1) The Al-Si coating would melt, flow and dissolve in the weld pool. This led to the increase in Al content in the fusion zone. For the 1-mm-thick sheet with 25 μm Al-Si coating, the average Al content was 2.5 wt.%. When the Al-Si layer was removed, the average Al content was only 0.5 wt.% in the fusion zone.
- (2) The low-Al weld had the following solidification process in the non-equilibrium condition: $L \rightarrow L + \gamma$. The high-Al weld had the following solidification process: $L \rightarrow L + \delta \rightarrow \delta \rightarrow \gamma + \delta$. The δ -ferrite showed a solidification morphology with an irregular shape.

- (3) After the heat treatment (950 °C for 5 min and then water-quenched), the lath martensite became finer in the de-coated weld due to the recrystallization and more ferrite formed in the coated weld.
- (4) The coated and de-coated joints had a similar tensile strength (585 MPa) and elongation (11-13%) in welded condition. However, compared with the de-coated joint, the coated joint showed a sharp reduction in strength and elongation in hot-stamped condition. The reduction was from 1482 to 1124 MPa in the strength and from 3 to 0.9% in the elongation. The reduction was caused by the formation of δ -ferrite. The brittle joint showed that the fracture surface had many cleavage planes.

Acknowledgments

This work received financial support from Baoshan Iron & Steel Co., Ltd. It was also supported by the Natural Science Foundation (NSF, Grant No. 51705318). This work was also supported by the Ministry of Industry and Information Technology of China under the project of LNG shipbuilding.

References

1. T. Senuma, Physical Metallurgy of Modern High Strength Steel Sheets, *ISIJ Int.*, 2001, **41**(6), p 520–532
2. H. Karbasian and A.E. Tekkaya, A Review on Hot Stamping, *J. Mater. Process. Technol.*, 2010, **210**(15), p 2103–2118. <https://doi.org/10.1016/j.jmatprotec.2010.07.019>
3. D.W. Fan and B.C. De Cooman, State-of-the-Knowledge on Coating Systems for Hot Stamped Parts, *Steel Res. Int.*, 2012, **83**(5), p 412–433
4. R.J. Pallett and R.J. Lark, The Use of Tailored Blanks in the Manufacture of Construction Components, *J. Mater. Process. Technol.*, 2001, **117**(1–2), p 249–254
5. R.S. Sharma and P. Molian, Yb:YAG Laser Welding of TRIP780 Steel with Dual Phase and Mild Steels for Use in Tailor Welded Blanks, *Mater. Des.*, 2009, **30**(10), p 4146–4155. <https://doi.org/10.1016/j.matdes.2009.04.033>
6. Z. Gu, S. Yu, L. Han, X. Li, and H. Xu, Influence of Welding Speed on Microstructures and Properties of Ultra-High Strength Steel Sheets in Laser Welding, *ISIJ Int.*, 2012, **52**(3), p 483–487
7. A. Pic, D. Múniera, L. Cretteur, F. Schmit, and F. Pinard, Innovative Hot-Stamped Laser Welded Blank Solutions, *Stahl Undsen*, 2009, **128**(8), p 59–66
8. C. Kim, M.J. Kang, and Y.D. Park, Laser Welding of Al-Si Coated Hot Stamping Steel, *Procedia Eng.*, 2011, **10**, p 2226–2231. <https://doi.org/10.1016/j.proeng.2011.04.368>
9. W. Ehling, L. Cretteur, A. Pic, R. Viestraete, and Q. Yin, Development of a Laser Decoating Process for Fully Functional Al-Si Coated Press Hardened Steel Laser Welded Blank Solutions, *Proceedings of 5th International WLT-Conference on Lasers in Manufacturing, Munich, Germany (AT-Fachverlag GmbH, Stuttgart)*, 2009, p. 409–416
10. R. Vierstraete, W. Ethling, F. Pinard, L. Cretteur, A. Pic, and Q. Yin, Laser Ablation for Hardening Laser Welded Steel Blanks, *Ind. Laser Solut.*, 2010, **25**(2), p 6
11. T. Flehmig, J. Gorschluter, and S. Wischmann, Method and Device for Mechanically Removing Coatings from Coated Blanks Using a Press and Scraping Knife, (Germany), US patent, 20140060281A1, 2014
12. T. Flehmig, D. Scheuevens, and L. Homig, Device and Method for Partial Decoating And/or Machining of Material from a Workpiece, (Germany), US patent, 20150239053A1, 2015
13. M. Kang, C. Kim, and S.M. Bae, Laser Tailor-Welded Blanks for Hot-Press-Forming Steel with Arc Pretreatment, *Int. J. Autom. Technol.*, 2015, **16**(2), p 279–283. <https://doi.org/10.1007/s12239>
14. M. Kang and C. Kim, Laser Welding for Hot-Stamped Tailor-Welded Blanks with High-Strength Steel/High-Energy Absorption Steel, *J. Laser Appl.*, 2014, **26**(3), p 32007. <https://doi.org/10.2351/1.4881279>
15. M. Kang, Y.M. Kim, and C. Kim, Effect of Heating Parameters on Laser Welded Tailored Blanks of Hot Press Forming Steel, *J. Mater. Process. Technol.*, 2015, <https://doi.org/10.1016/j.jmatprotec.2015.06.028>
16. M. Windmann, A. Röttger, and W. Theisen, Formation of Intermetallic Phases in Al-Coated Hot-Stamped 22MnB5 Sheets in Terms of Coating Thickness and Si Content, *Surf. Coat. Technol.*, 2014, **246**, p 17–25
17. P. Mayr, T.A. Palmer, J.W. Elmer, E.D. Specht, and S.M. Allen, Formation of Delta Ferrite in 9 Wt Pct Cr Steel Investigated by in-Situ X-Ray Diffraction Using Synchrotron Radiation, *Metall. Mater. Trans. A Phys. Metall. Mater. Sci.*, 2010, **41**(10), p 2462–2465
18. S.H. Kim, H.K. Moon, T. Kang, and C.S. Lee, Dissolution Kinetics of Delta Ferrite in AISI, 304 Stainless Steel Produced by Strip Casting Process, *Mater. Sci. Eng. A*, 2003, **356**(1–2), p 390–398
19. G. Lothongkum, E. Vivanit, and P. Bhandhubanyong, Study on the Effects of Pulsed TIG Welding Parameters on Delta-Ferrite Content, Shape Factor and Bead Quality in Orbital Welding of AISI, 316L Stainless Steel Plate, *J. Mater. Process. Technol.*, 2001, **110**(2), p 233–238
20. A. De, C.A. Walsh, S.K. Maiti, and H.K.D.H. Bhadeshia, Prediction of Cooling Rate and Microstructure in Laser Spot Welds, *Sci. Technol. Weld. Join.*, 2003, **8**(6), p 391–399
21. X. Wang, H. Li, Z. Liu, H. Liu, G. Wang, Z. Luo, F. Zhan, S. Chen, and L. Lyu, Effect of Cooling Rate on Bending Behavior of 6.5 wt.% Si Electrical Steel Thin Sheets Fabricated by Strip Casting and Rolling, *Mater. Charact.*, 2016, **111**, p 67–74. <https://doi.org/10.1016/j.matchar.2015.11.008>
22. S.S. Babu, J.W. Elmer, J.M. Vitek, and S.A. David, Time-Resolved X-Ray Diffraction Investigation of Primary Weld Solidification in Fe-C-Al-Mn Steel Welds, *Acta Mater.*, 2002, **50**(19), p 4763–4781
23. S.S. Babu, J.M. Vitek, J.W. Elmer, T.A. Palmer, and S.A. David, “Nonequilibrium Phase Selection During Weld Solidification of Fe-C-Mn-Al,” *TMS (The Minerals, Metals & Materials Society)*, 2004, p 5
24. S. Katayama and A. Matsunawa, Solidification Microstructure of Laser Welded Stainless Steels, *Proceedings of Material Processing Symposium; Laser Institute of America. ICALAO*, 1984, p 60–67
25. J.W. Elmer, S.M. Allen, and T.W. Eagar, Microstructural Development during Solidification of Stainless Steel Alloys, *Metall. Trans. A*, 1989, **20**(October), p 2117–2131
26. C.Y. Lee and Y.K. Lee, The Solidification Mode of Fe-Mn-Al-C Lightweight Steel, *JOM*, 2014, **66**(9), p 1794–1799. <https://doi.org/10.1007/s11837-014-1000-5>
27. L. Schafer, Influence of Delta Ferrite and Dendritic Carbides on the Impact and Tensile Properties of a Martensitic Chromium Steel, *J. Nucl. Mater.*, 1998, **263**, p 1336–1339
28. P. Wang, S.P. Lu, N.M. Xiao, D.Z. Li, and Y.Y. Li, Effect of Delta Ferrite on Impact Properties of Low Carbon 13Cr-4Ni Martensitic Stainless Steel, *Mater. Sci. Eng. A*, 2010, **527**(13–14), p 3210–3216. <https://doi.org/10.1016/j.msea.2010.01.085>
29. M. Kang, C. Kim, and J. Lee, Weld Strength of Laser-Welded Hot-Press-Forming Steel, *J. Laser Appl.*, 2012, **24**(2), p 22004